



Precipitation hardening behavior and microstructure evolution of Al–5.1 Mg–0.15Cu alloy with 3.0Zn (wt%) addition

Shengli Hou¹, Pingping Liu², Di Zhang^{1,*} , Jishan Zhang¹, and Linzhong Zhuang^{1,3,*}

¹ State Key Laboratory for Advanced Metals and Materials, University of Science and Technology Beijing, Beijing 100083, People's Republic of China

² School of Materials Science and Engineering, University of Science and Technology Beijing, Beijing 100083, People's Republic of China

³ TaTa Steel, 1970 CA IJmuiden, The Netherlands

Received: 24 August 2017

Accepted: 9 November 2017

Published online:
20 November 2017

© Springer Science+Business
Media, LLC, part of Springer
Nature 2017

ABSTRACT

The precipitation hardening behavior of Al–5.1Mg–0.15Cu alloy with 3.0Zn (wt%) addition at various temperatures has been systematically investigated in this study. The Al–5.1Mg–0.15Cu–3.0Zn alloy possesses the higher strength compared with traditional Zn-free alloy, when the alloy is treated at 363 K for 24 h and subsequently aged at 413 K for 25 h. The precipitation sequence of the hardening phase T-Mg₃₂(AlZn)₄₉ is investigated by differential scanning calorimetry tests, transmission electron microscopy and high-resolution electron microscopy. The different effects of natural aging and pre-aging on the precipitation hardening behavior are detailed. The formation of relatively stable Guinier–Preston zones of T-Mg₃₂(AlZn)₄₉ phase during pre-aging rather than natural aging results in higher mechanical strength during subsequent artificial aging at relatively high temperatures. When the Al–5.1Mg–0.15Cu–3.0Zn alloy is aged at 453 K, the peak hardness is from synergetic effect of hardening of S-Al₂CuMg phase and coarsening of T phase. However, during two-step artificial aging treatment, the peak hardness results from fine, spherical and homogeneously distributed T phase in the absence of the S phase.

Introduction

Traditional 5 × × × series Al–Mg alloys are used extensively in marine and armor vehicle transportation due to their excellent corrosion resistance, weldability, formability and high strength to weight

ratio [1, 2]. The possible precipitation sequence of this alloy can be summarized as: supersaturated solid solution (SSSS) → GP zone I → GP zone II (β'') → intermediate phase β' → equilibrium phase β (Al₃Mg₂) [3–5]. However, this alloy could not be strengthened by precipitation hardening, mainly

Address correspondence to E-mail: zhangdi@skl.ustb.edu.cn; linzhongzhuang@yahoo.com

because GP zones or precipitates are easier to occur along grain boundaries and dislocations rather than homogeneous precipitation in the matrix after quenching [6]. Therefore, the strength of $5 \times \times \times$ series alloy is significantly lower compared with precipitation hardening alloys, such as $2 \times \times \times$ and $7 \times \times \times$ series alloys. Traditional methods to improve the strength of $5 \times \times \times$ series alloys include the addition of large amounts of Mg and the larger plastic deformation, because the alloy is typically strengthened by solid solution strengthening and work hardening [7]. Unfortunately, they may deteriorate the corrosion resistance and hot deformation behavior of the alloy.

In recent years, dispersion hardening and precipitation hardening have been introduced in traditional $5 \times \times \times$ series Al–Mg alloys by the addition of other alloying elements. The additions of Sc, Zr and Er dramatically increase the yield strength, fatigue strength, thermal stability and creep resistance of the $5 \times \times \times$ series Al–Mg alloys as well as the strength of the as-welded alloy by the formation of nano-sized and coherent Al_3Sc , $\text{Al}_3(\text{ScZr})$ [8–10], Al_3Er and $\text{Al}_3(\text{ErZr})$ precipitates [11–13]. Stable precipitates strongly pin the dislocations and prevent their slips, migration and incorporation to grain boundaries or sub-grain boundaries. However, the addition of rare earth elements may be unacceptable in commercial applications due to their cost. According to previous studies, trace Cu has been considered to be effective to control the microstructure and increase the mechanical strength of the alloys due to the heterogeneous precipitation of $S''\text{-Al}_2\text{CuMg}$ phase on dislocation loops and helices during artificial aging treatment [14–17]. It is effective to offset the paint bake softening after the press forming of traditional $5 \times \times \times$ series Al–Mg alloys in automobile industry. Unfortunately, higher amount of Cu may strongly deteriorate the corrosion resistance of the alloy due to the anodic dissolution of Cu-depleted zones adjacent to grain boundaries. Further addition of Si enhances the age-hardening response of the Al–Mg–Cu alloy, mainly because Si consumes significant amount of Mg and Cu atoms and stabilizes the formation of GPB (Guinier–Preston–Bagaryasky) zones [18]. However, the insoluble particles may deteriorate the ductility of Si-modified alloys [19, 20]. Small addition of Ag (0.4 wt%) can also increase the strength of the alloys by the formation of heterogeneous T-Mg₃₂(AlCuAg)₄₉ phases during artificial aging treatment

[21–24]. An obvious age-hardening behavior was also observed in Al–Mg alloy with Ga addition [25]. However, the cost of Ag and Ga made the alloys infeasible for industrial applications.

The Zn addition can significantly improve the precipitation kinetics and age-hardening response through decreasing activation energy of $\beta''\text{-Mg}_2\text{Si}$ phases or precipitating $\eta'\text{-MgZn}_2$ phases in Al–Mg–Si–Cu alloys [26, 27]. The addition of Zn to traditional $5 \times \times \times$ series Al–Mg alloys was pioneered by Carroll et al. [28, 29]. According to their study, 0.4–1.0 Zn (wt%) addition dramatically enhanced the corrosion resistance due to the formation of T-Mg₃₂(AlZn)₄₉ precipitates in grain boundary. However, the detailed information of T-Mg₃₂(AlZn)₄₉ in grain was not given. The effect of 0.4 Zn (wt%) addition on the age-hardening behavior of the Al–Mg–Cu alloy was studied, and the increment of hardness was 10 HV during artificial aging for 10000 min compared with the Zn-free alloy [30]. Matsumoto et al. have investigated Al–6Mg alloy with 2.8Zn (wt%) and discovered that the yield strength reached 270 MPa during artificial aging at 423 K for 24 h compared with 140 MPa at the as-quenched state, which was attributed to the formation of Zn–Mg clusters during artificial aging [31, 32]. Researchers have demonstrated that in $7 \times \times \times$ series Al alloy, the main strengthening phase was modified by Zn–Mg atom ratio, which can be summarized as the fact that $\eta\text{-MgZn}_2$ is the primary strengthening phase when Zn–Mg atom ratio is over 2.2 during artificial aging, while body-centered cubic T-Mg₃₂(AlZn)₄₉ is the primary strengthening phase when the atom ratio is below 2.2 [33]. A preliminary study by Bigot [34] showed that the composition of equilibrium T phase was close to 36.5 at.% Mg, 36.5 at.% Al and 26 at.% Zn, and the differences between equilibrium T phase and its early precursor T' could be distinguished by their chemical compositions. According to the previous study about a Cu-free $7 \times \times \times$ series Al alloy, both equilibrium T and its precursor T' were coherent with the Al matrix [35]. However, they only can gain the fact that Zn addition can improve the strength of Al–Mg alloys due to the formation of T phase. Up to the present, detailed information of precipitation hardening processing and microstructure evolution for Al–Mg–Cu–Zn alloys in different aging conditions has not been presented systematically.

Therefore, this study systematically investigates more detailed precipitation sequence of T phase and

properties of T phase in different states. The precipitation processing in different aging conditions (single aging, two-step aging and natural aging) and the effects of natural aging and pre-aging treatment on designed alloy also have been studied. In addition, altered precipitation behavior in single- and two-step aging is discussed in details. These results are of great importance for future design and possibly provide a guide to the development of Al–Mg–Cu–Zn alloys.

Experimental procedures

Materials and heat treatment

Table 1 shows the nominal chemical compositions of the Al–Mg–Cu–(Zn) alloys in this study. The materials include a reference Zn-free alloy (Alloy 1) and a designed alloy with 3.0 Zn (wt%) (Alloy 2), respectively. The alloys were prepared by melting and chill casting into a steel mold with circulation water. The ingots were homogenized, scalped, hot rolled, recrystallized and cold rolled to a thickness of 5 mm. Samples were solution treated at 803 K for 10 min in a salt bath, followed by immediate quenching in cold water and divided into three groups. One group of samples was directly aged at 363, 413, 453 and 493 K, respectively. The second group of samples was aged at 363 K for 24 h and then aged at 363, 413, 453, 473 and 493 K, respectively. The last group of samples was naturally aged for 168 and 720 h, respectively, and then artificially aged at 453 K.

Mechanical measurements and differential scanning calorimetry tests

Hardness measurements were taken by using a macro-Vickers hardness tester (Wolpert-401MVD) with a load of 200 g and a dwelling time of 15 s on the longitudinal-short transverse surface. Each reported hardness value is the average of 10 indi-

vidual measurements to ensure reproducibility. The tensile specimens were taken in the rolling direction with a gauge length of 25 mm and a width of 6 mm. The tensile properties of aged specimens were tested at room temperature with an initial strain rate of $4.8 \times 10^{-4} \text{ s}^{-1}$. Each reported tensile testing value was the average of three individual tests. Differential scanning calorimetry (DSC) tests were performed on NETZSCH DSC 214 instrument in a nitrogen atmosphere with a heating rate of 5 K min^{-1} .

Microstructure observation

Foils of 3-mm disks for transmission electron microscopy (TEM) observation were thinned by the twin-jet electro-polishing in a 25 vol% nitric acid and 75 vol% methanol at temperatures between 243 and 238 K. Bright field (BF) TEM and high-resolution transmission electron microscopy (HRTEM) studies were carried out on the alloys with JEOL-2010 and FEI Tecnai-F20. Energy-dispersive spectroscopy (EDS) was employed to explore the distribution of Al, Mg, Zn, Cu and Mn elements during artificial aging. An inverse fast fourier transformation (IFFT) pattern was obtained to distinguish coherent relationship along the interface of precipitates and Al matrix. Image-Pro Plus analysis software has been employed to reveal the number density and average diameter of precipitates during different aging treatments. We assume that the shape of phases is sphere like when computing the average diameter. The thickness of the statistical region measured through electron energy-loss spectrometry (EELS) is about 70 nm, and the number density can be obtained by their total number dividing the volume. In order to ensure a reasonable accuracy, these TEM images under the same conditions were used to estimate the number density and the average diameter of precipitates.

Table 1 Nominal chemical compositions of the two alloys (wt%)

Element	Zn	Mg	Mn	Ti	Si	Zr	Cu	Fe	Cr	Al
Alloy 1 (Al–5.1Mg–0.15Cu)	0	5.1	0.80	0.07	0.15	0.15	0.15	0.20	0.03	Balance
Alloy 2 (Al–5.1Mg–0.15Cu–3.0Zn)	3.0	5.1	0.80	0.07	0.15	0.15	0.15	0.20	0.03	Balance

Results

Precipitation hardening behavior during different aging treatments

Figure 1 shows the hardness curves plotted against the aging time for Alloy 2 (Al–5.1Mg–0.15Cu–3.0Zn) at various artificial aging temperatures. Both the peak hardness and the time of reaching the peak hardness decrease with an increase of artificial aging temperature. The hardness value reaches 155 HV when the alloy is aged at 363 K for 550 h. The peak hardness for 493 K appears when the alloy is aged for 2 h. But the peak hardness value is only 102 HV, much lower than that aged at 363 K. The hardness value is 130 HV during natural aging for 6000 h, and it still increases with mounting natural aging time.

Figure 2 shows the hardness curves for Alloy 2 which are aged at 363 K for 24 h and subsequently aged at different aging temperatures. During the second-step aging treatment, the hardness value and the time of reaching the peak hardness decrease with the increase in aging temperature. The hardness value is 155 HV when the alloy is aged at 413 K for 25 h after a pre-aging at 363 K for 24 h. With the increase in the second aging temperature, the age-hardening response is improved, but the peak hardness decreases.

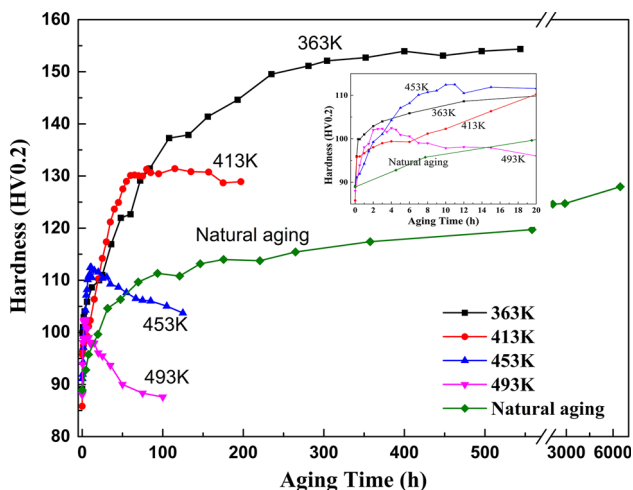


Figure 1 Hardness curves for Alloy 2 during natural aging and artificial aging at 363, 413, 453 and 493 K, respectively.

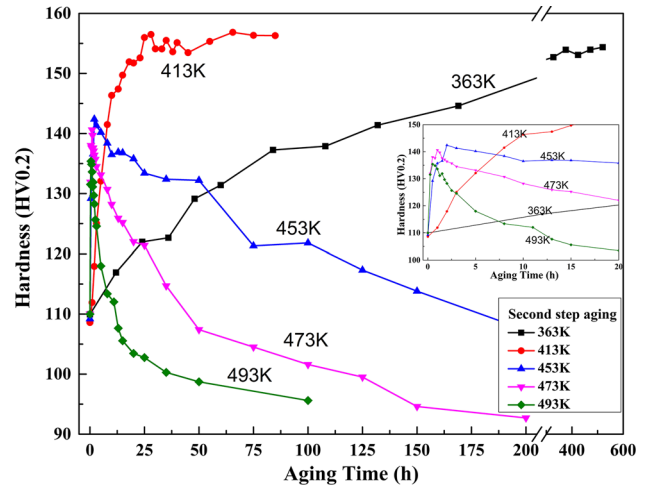


Figure 2 Hardness curves for Alloy 2 aged at 363 K for 24 h and subsequently aged at 413, 453, 473 and 493 K, respectively.

Effects of Zn addition on the precipitation hardening behavior

Figure 3a, b shows the effect of Zn addition on the precipitation hardening behavior of Al–Mg–Cu alloy during natural aging and artificial aging at 413 K after pre-aging at 363 K for 24 h. It shows that the hardening effect can be neglected for the Zn-free alloy (Alloy 1). Both the peak hardness value and age-hardening response are improved with 3.0 Zn (wt%) addition. The hardness increment reaches 40 HV for natural aging and 65 HV for two-step aging treatment (363 K/24 h + 413 K/25 h) for Alloy 2.

Figure 3c–f exhibits the effect of Zn addition on the mechanical properties in the precipitation hardening temper (363 K/24 h + 413 K/25 h). Both the yield and tensile strength increase with Zn addition, whereas the elongation decreases. The above results show that artificial aging at 413 K for 25 h after pre-aging at 363 K for 24 h is an optimized aging treatment for Alloy 2.

Precipitation sequence of T-Mg₃₂(AlZn)₄₉

Figures 4, 5, 6 and 7 show the BF TEM microstructure, selected area diffraction (SAD), HRTEM and IFFT images of Alloy 2 during different artificial aging treatments. The electron beam in each figure approximately parallels to $\langle 100 \rangle$ zone axis. In this study, the microstructures of four typical artificial aging treatments which represent the under-aged state (363 K/24 h), peak-aged state (363 K/

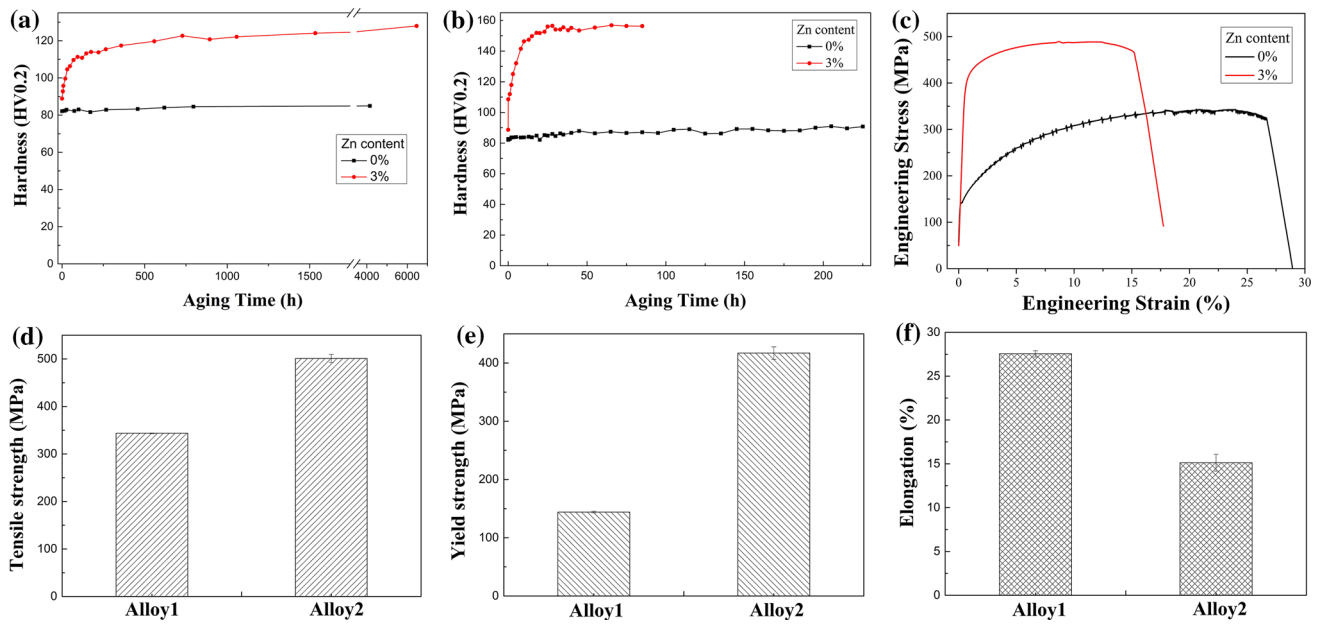


Figure 3 Hardness curves for the two alloys during natural aging (a) and artificial aging at 363 K for 24 h and subsequently aged at 413 K (b). Mechanical properties for the two alloys aged at 363 K

for 24 h and subsequently aged at 413 K: c stress–strain curves, d tensile strength, e yield strength and f elongation.

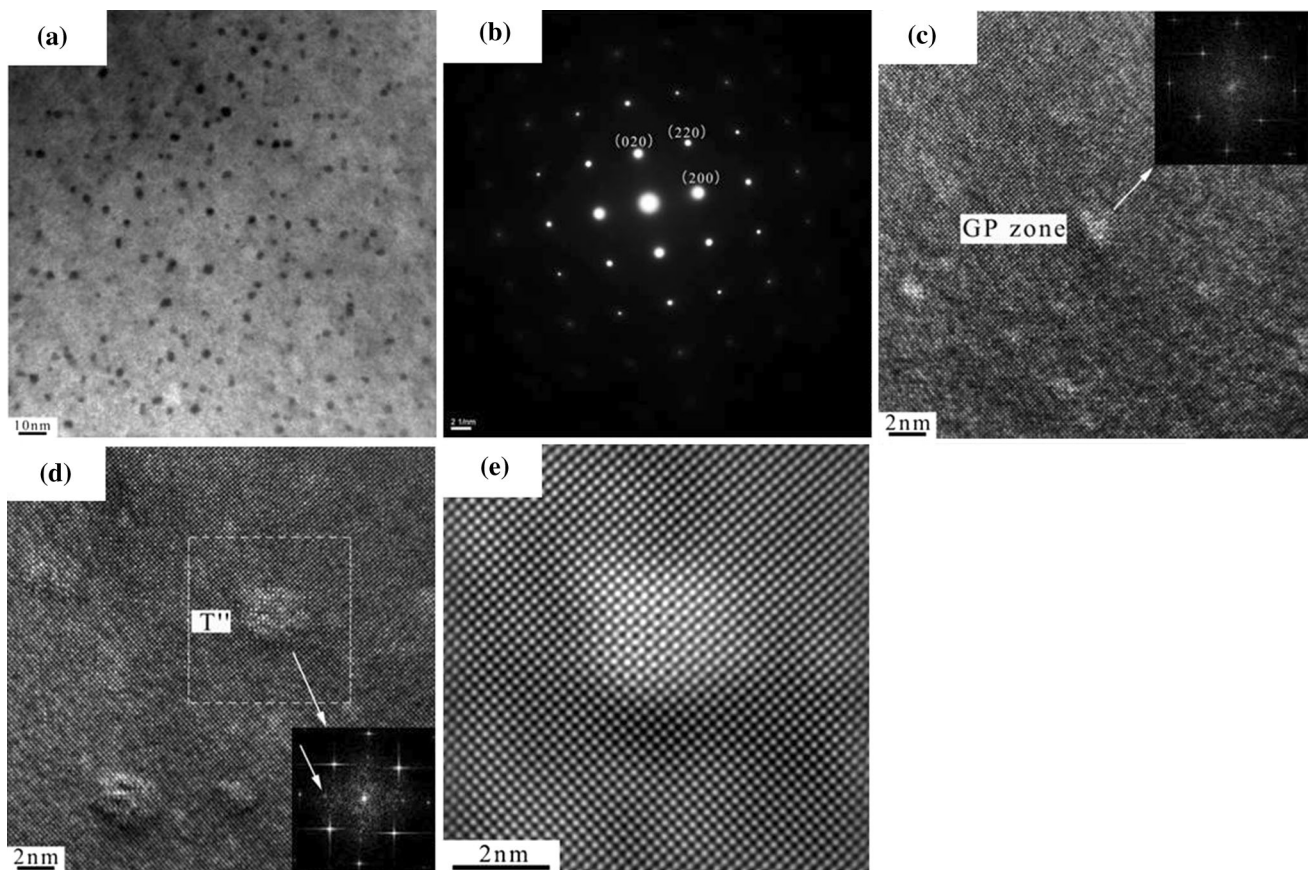


Figure 4 TEM microstructure for Alloy 2 under-aged at 363 K for 24 h: a BF TEM image; b corresponding SAD pattern of a; c, d HRTEM image; e corresponding IFFT pattern of d.

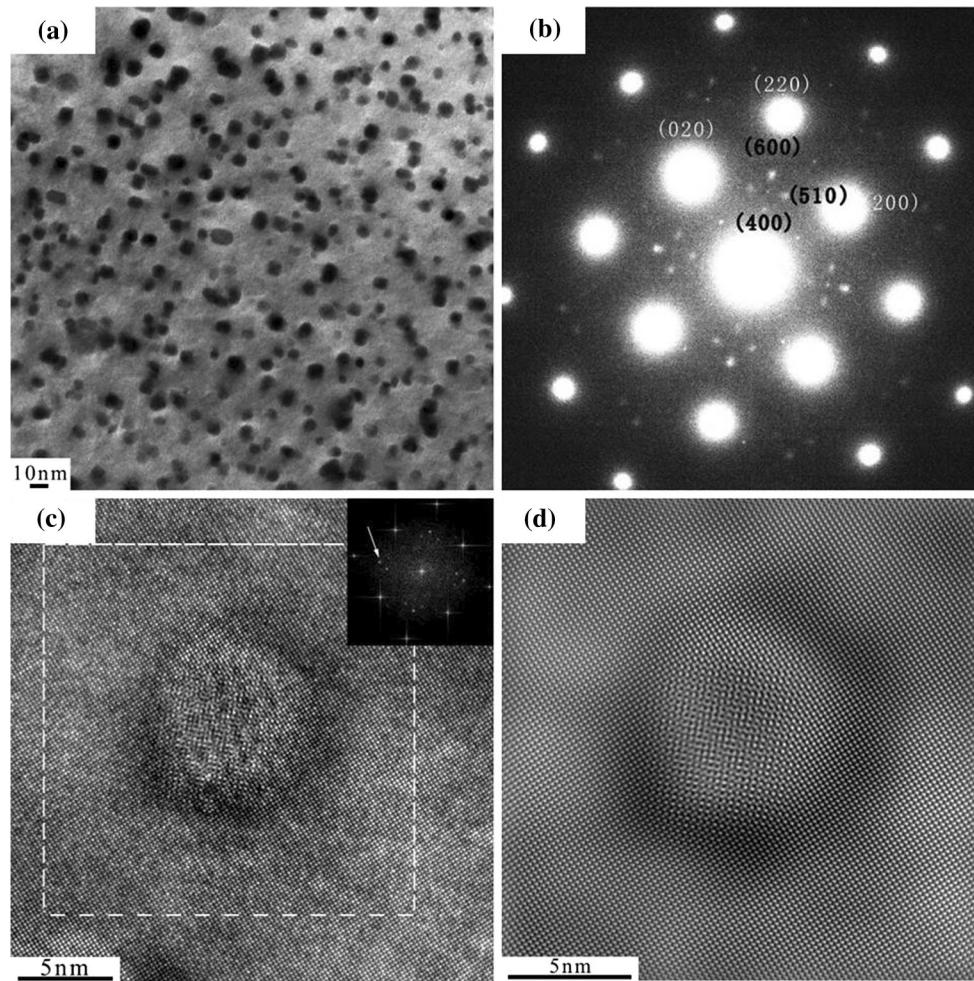


Figure 5 TEM microstructure for Alloy 2 peak aged at 363 K for 24 h and subsequently aged at 413 K for 25 h: **a** BF TEM image; **b** corresponding SAD pattern of **a**; **c** HRTEM image; **d** corresponding IFFT pattern of **c**.

24 h + 413 K/25 h), over-aged state (363 K/24 h + 453 K/100 h) and highly over-aged state (363 K/24 h + 473 K/200 h) are observed to investigate the precipitation sequence of T-Mg₃₂(AlZn)₄₉ in Alloy 2. The temperature selected for over-aged state is higher than that for peak-aged state. This is mainly because the current alloy over-ages quite slowly, and over aging can be accelerated at higher temperatures. Table 2 presents the morphology, average diameter, density of the precipitates and coherent relationship with the matrix of the precipitates during different artificial aging treatments.

During under-aged treatment at 363 K for 24 h, the microstructure contains fine, sphere-like and homogeneously dispersed particles as shown in the BF TEM and HRTEM images (Fig. 4a, c, d). There is no extra spot except for the spots of Al matrix from the SAD in Fig. 4b, which indicates that GP zones are the

main particles in the under-aged state. No obvious diffraction patterns of the sphere-like particles can be observed in the FFT pattern as shown in Fig. 4c, which suggests that no unique and distinctive structure is formed in this state. These smaller sphere-like particles appear possibly due to the formation of GP zones of Mg–Zn clusters, which are fully coherent with the Al matrix. In another HRTEM image, however, diffraction spots of the precipitate are clearly stated in Fig. 4d. In addition, the precipitate is fully coherent with the Al matrix, which is shown in the IFFT image (Fig. 4e). The average diameter of precipitates is slightly larger than that of GP zones. It is believed that with an increase of aging time in the under-aged state, GP zones which have reached a sufficient large radius evolve into sphere-like precipitates. Due to the above results, we define the above small cluster as GPI zone, and the larger

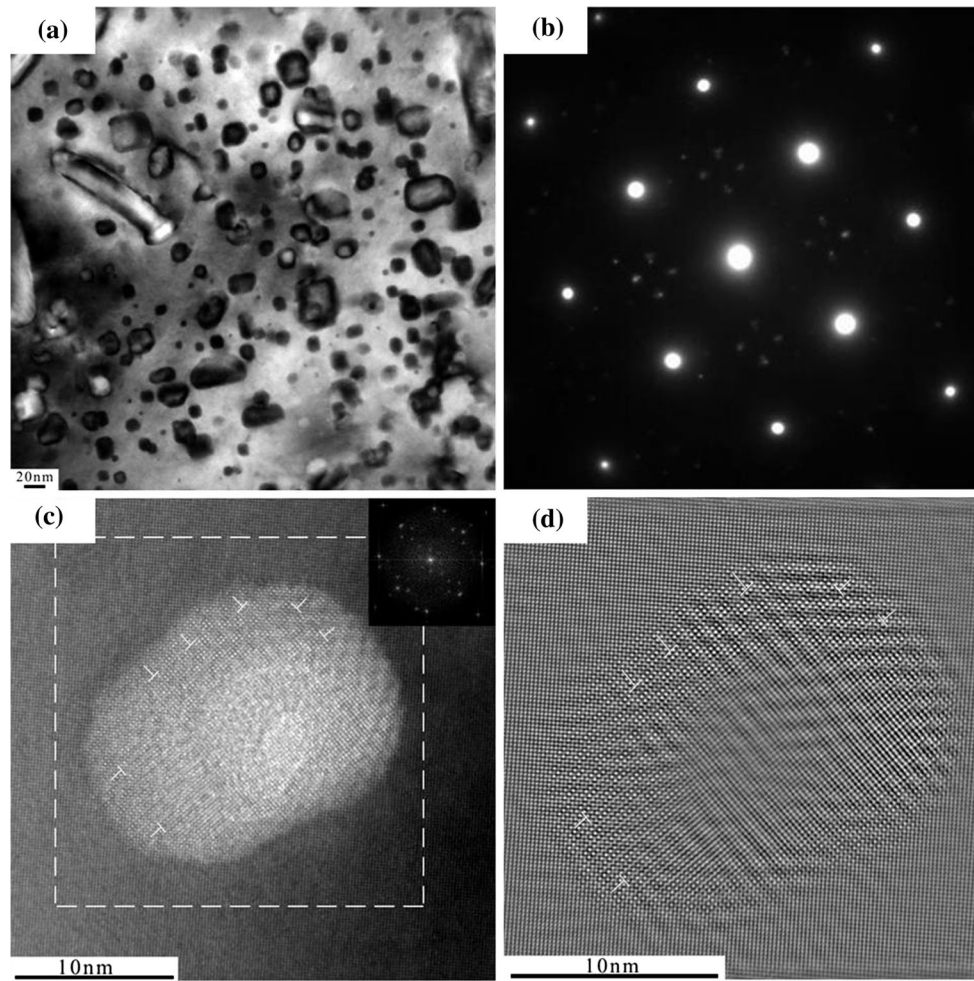


Figure 6 TEM microstructure for Alloy 2 over-aged at 363 K for 24 h and subsequently aged at 453 K for 100 h: **a** BF TEM images; **b** corresponding SAD pattern of **a**; **c** HRTEM image; **d** corresponding IFFT pattern of **c**.

cluster with diffraction spots as GPII zone or T'' phase. Statistic results show that GP zones and precipitates have an average diameter of 2 nm and a density of 200 per μm^3 in this state.

Figure 5a displays the BF TEM microstructure of Alloy 2 in peak-aged state. It shows that the fine and sphere-like precipitates grow larger. The average diameter of precipitates reaches 6 nm, and the density of precipitates decreases to 122 per μm^3 compared with that of the under-aged state. In Fig. 5b, c, the SAD and corresponding FFT (inset) of the HRTEM exhibit intensity at $2/5$ and $3/5$ $\langle 220 \rangle_{\text{Al}}$ which can be identified as the $\text{T-Mg}_{32}(\text{AlZn})_{49}$ phase ($\text{Im}3$, $a = 1.422$ nm). The orientation relationship of the $\text{T-Mg}_{32}(\text{AlZn})_{49}$ phase with the matrix can be described as $(100)_{\text{T}} // (110)_{\text{Al}}$ and $(110)_{\text{T}} // (010)_{\text{Al}}$ which is in good agreement with the results reported by Loffler et al. [36]. In Fig. 5c, d, it is evident that the

precipitates are coherent with the Al matrix, but the atom lattices have been severely distorted.

Figure 6a shows the BF TEM microstructure of Alloy 2 in over-aged state. Both spherical-like precipitates and polygonal-like precipitates are simultaneously observed in over-aged state. In Fig. 6b, c, the SAD and corresponding FFT (inset) of the HRTEM prove that both spherical-like and polygonal-like precipitates are characterized as $\text{T-Mg}_{32}(\text{AlZn})_{49}$ phase. Precipitates grow further and the density of precipitates decreases which may be the reason of the decrease in hardness. An array of lattice planes in precipitates terminates at the interface, and thus an array of edge dislocations is formed, as indicated by “ \perp ” along the interface as shown in the HRTEM and IFFT images in Fig. 6c, d. The precipitates are semi-coherent with the matrix.

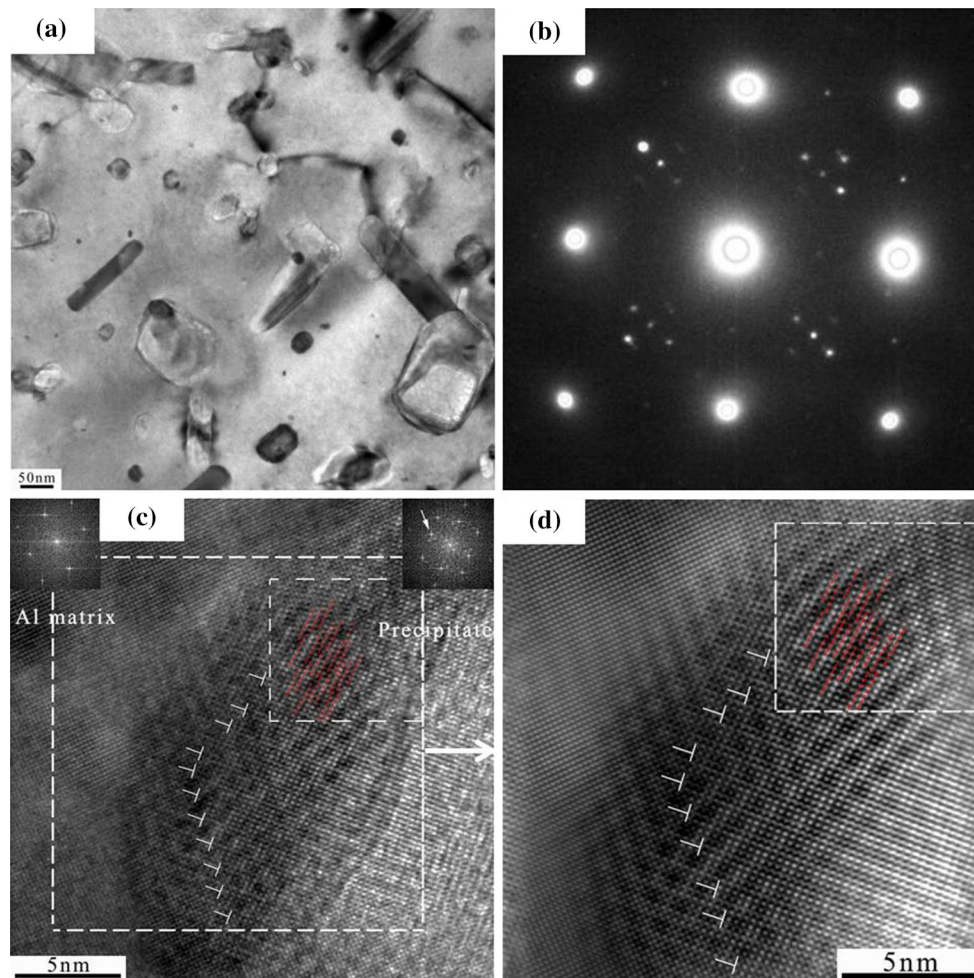


Figure 7 TEM microstructure for Alloy 2 highly over-aged at 363 K for 24 h and subsequently aged at 473 K for 200 h: **a** BF TEM image; **b** corresponding SAD pattern of **a**; **c** HRTEM image; **d** corresponding IFFT patterns of **c**.

Table 2 Characteristic information of T phase corresponding to the precipitation sequence

	Hardness (HV)	Morphology	Average diameter (nm)	Number density (number/ μm^3)	Coherent relationship	Precipitation sequence
Under age	110	Sphere like	2 ± 0.6	200	Full coherent	GPI zones or GPII zones (T'')
Peak age	155	Sphere like	6 ± 1.8	122	Coherent with serious strain	GPII zones (T'')
Over age	122	Sphere like or polygonal like	14 ± 8.7	19	Semi-coherent	T'
Highly over age	93	Polygonal like or rod like	49 ± 32.4	1.2	Semi-coherent or incoherent	T

Figure 7a reveals the BF TEM microstructure of Alloy 2 in highly over-aged state. It is shown that these particles are dominated by both polygonal-like and rod-like precipitates. Although the morphology

of precipitates is dramatically changed during artificial aging treatment, the precipitates are still characterized as $T\text{-Mg}_{32}(\text{AlZn})_{49}$ phase as shown in the SAD (Fig. 7b) and corresponding FFT (inset) of the

HRTEM (Fig. 7c). The average diameter of precipitates reaches 49 nm, and their density decreases to $1.2 \mu\text{m}^3$ in this state. Figure 7c shows the HRTEM image of the interface between the matrix and precipitate. Figure 7d is the corresponding IFFT pattern from the area labeled by the larger white square in Fig. 7c. As shown in the figures, the precipitates are semi-coherent or incoherent with the Al matrix in the highly over-aged state. Figure 8 shows the EDS line scan of the precipitates artificially aged at 473 K for 200 h after pre-aging at 363 K for 24 h. It proves that the T-Mg₃₂(AlZn)₄₉ phase in this state is an Al-Mg-Zn-Cu phase homogeneously nucleated in the matrix (Fig. 8a) or heterogeneously nucleated along the

interface of Al-Mn precipitate (Fig. 8c), which is in good agreement with the results reported by Meng et al. [37].

The DSC curve of Alloy 2 in as-quenched state after solid solution treatment is shown in Fig. 9. There are four major exothermic peaks and one endothermic peak. Exothermal peak A around 333 K represents the formation of GPI zones. Exothermal peak B around 503 K represents the transformation of GPI zone \rightarrow GPII zone (T''), while exothermal peak C around 573 K means the transformation of $T'' \rightarrow T'$. Exothermal peak E around 703 K means the transformation of $T' \rightarrow T$. Endothermic peak D around

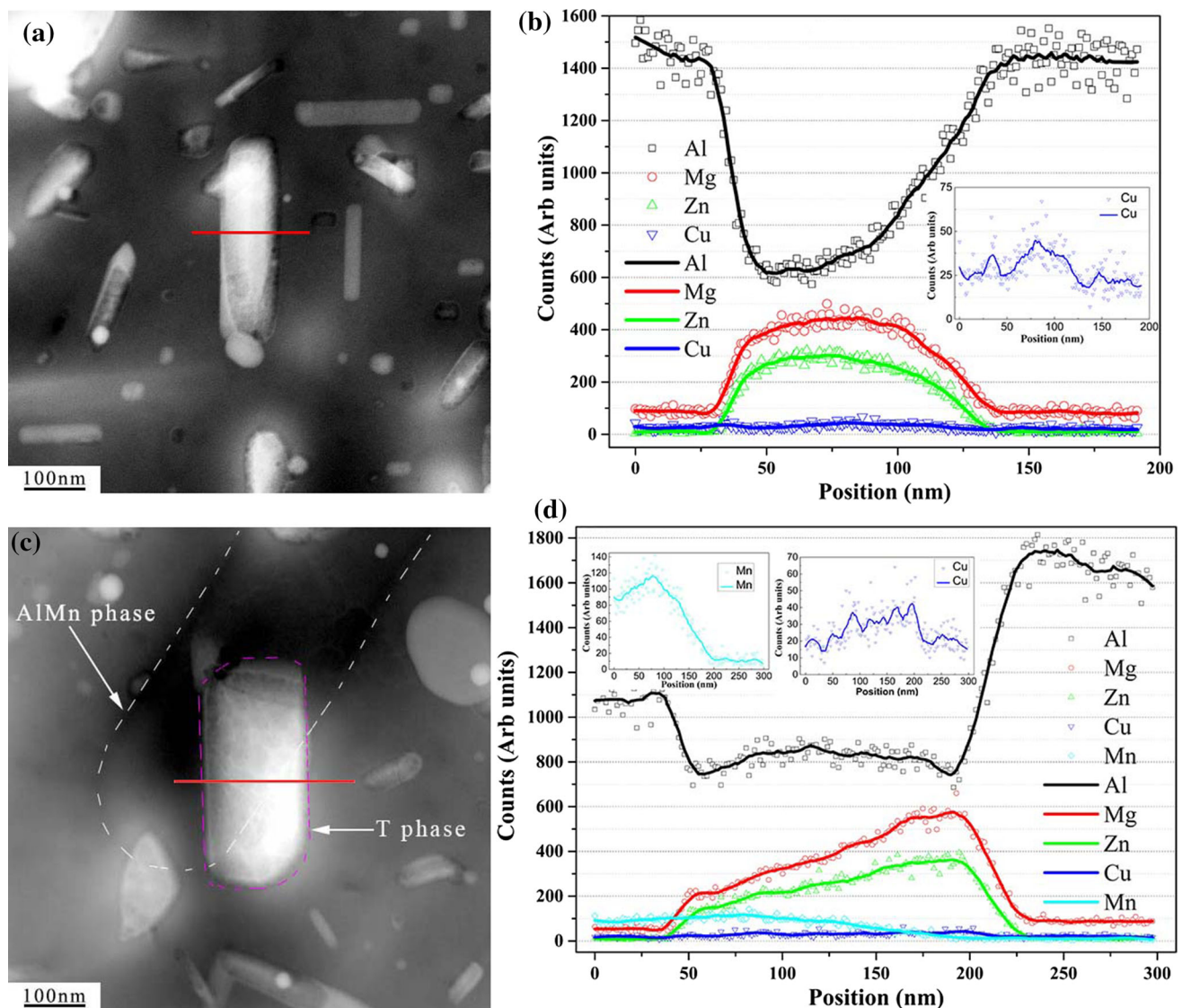


Figure 8 TEM images and EDS line scan across the precipitates for Alloy 2 aged at 363 K for 24 h and subsequently aged at 473 K for 200 h.

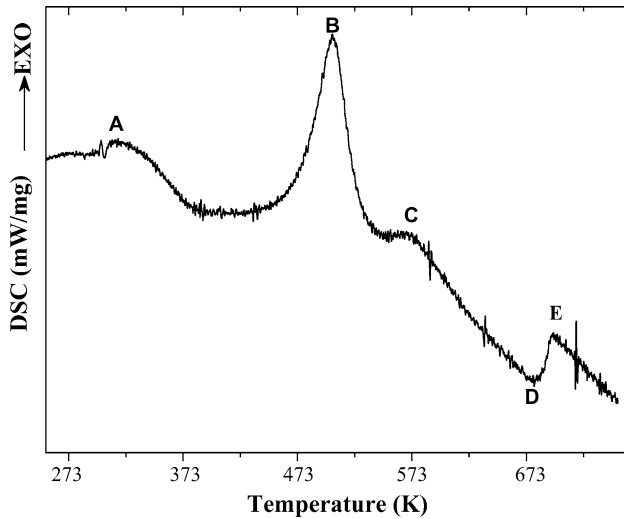


Figure 9 DSC curve for Alloy 2 after solution treatment.

673 K may be attributed to the dissolution of T' phase with small diameter.

Effect of first-step aging (natural aging and pre-aging) on the subsequent artificial aging treatment

Figure 10 indicates the hardness curves for Alloy 2 which is aged at 453 K only and heat-treated at 453 K after natural aging for 168 h or after pre-aging at 363 K for 24 h. The hardness value remains almost the same after natural aging for 168 h, pre-aging at 363 K for 24 h or single step aged at 453 K for 10.5 h. It is interesting to note that the hardness value of natural aging for 168 h suddenly decreases from 110

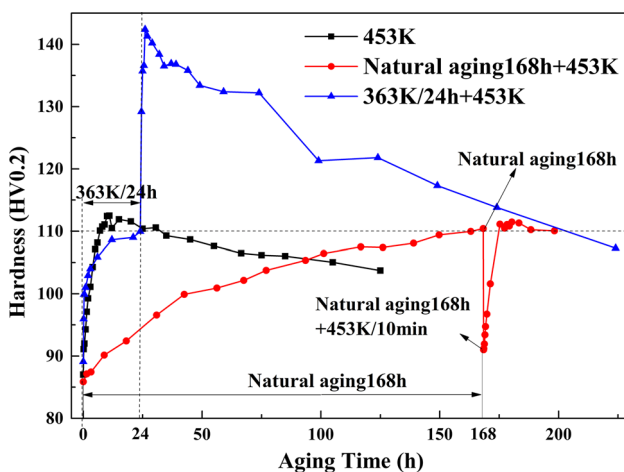


Figure 10 Hardness curves for Alloy 2 aged at 453 K after natural aging, single-step aging at 453 K and two-step aging at 363 K for 24 h and then 453 K, respectively.

to 90 HV within 10 min during the second-step aging at 453 K and then increases to the peak (110 HV) with artificial aging time. The hardness curve of the second step aged at 453 K after natural aging is similar to that of single step aged at 453 K. But after pre-aging at 363 K for 24 h, the hardness value quickly increases from 110 to 143 HV within 2 h. The results show that natural aging has no effect on the precipitation hardening behavior and the peak hardness for Alloy 2 aged at 453 K. The pre-aging is more efficient in increasing the strength than natural aging during aging at 453 K for Alloy 2. Additionally, the pre-aging can increase the peak hardness significantly and improve the age-hardening response greatly during subsequently aging at 453 K compared with the single aging at 453 K.

Microstructure characteristics of single-step aging, two-step aging and natural aging for Alloy 2

Figure 11a indicates the BF TEM images and SAD (inset) of Alloy 2 aged at 453 K for 2 h after pre-aging at 363 K for 24 h and shows that fine, sphere-like and uniformly distributed T-Mg₃₂(AlZn)₄₉ precipitates present in the matrix. In the SAD (inset) from Fig. 11a, diffraction spots of S-Al₂CuMg are absent, which may be due to the fact that the number density of S-Al₂CuMg is very low or there is no S-Al₂CuMg. Figure 11b–e shows BF TEM and HRTEM images of Alloy 2 and EDS lines scan of the precipitates single step aged at 453 K for 10.5 h. Both coarse rod-like T-Mg₃₂(AlZn)₄₉ precipitates and fine rod-like S-Al₂CuMg precipitates are simultaneously observed. The T phase in this state contains Al, Mg and Zn element without Cu, which is different from that in highly over-aged state after pre-aging (Fig. 8). As shown in Table 3, the average diameter of T-Mg₃₂(AlZn)₄₉ phase observed for the single-step aging is much higher than that of two-step aging, while the number density of the precipitates is much less than that observed at two-step aging state.

Figure 12a–d shows the BF TEM and HRTEM images for Alloy 2 naturally aged for 168 and 720 h, and the particles are clearly observed during natural aging for 168 and 720 h. However, the statistical results in Table 3 illustrate that smaller diameter and larger density of particles are observed during natural aging compared with those during pre-aging at 363 K for 24 h (Fig. 4a).

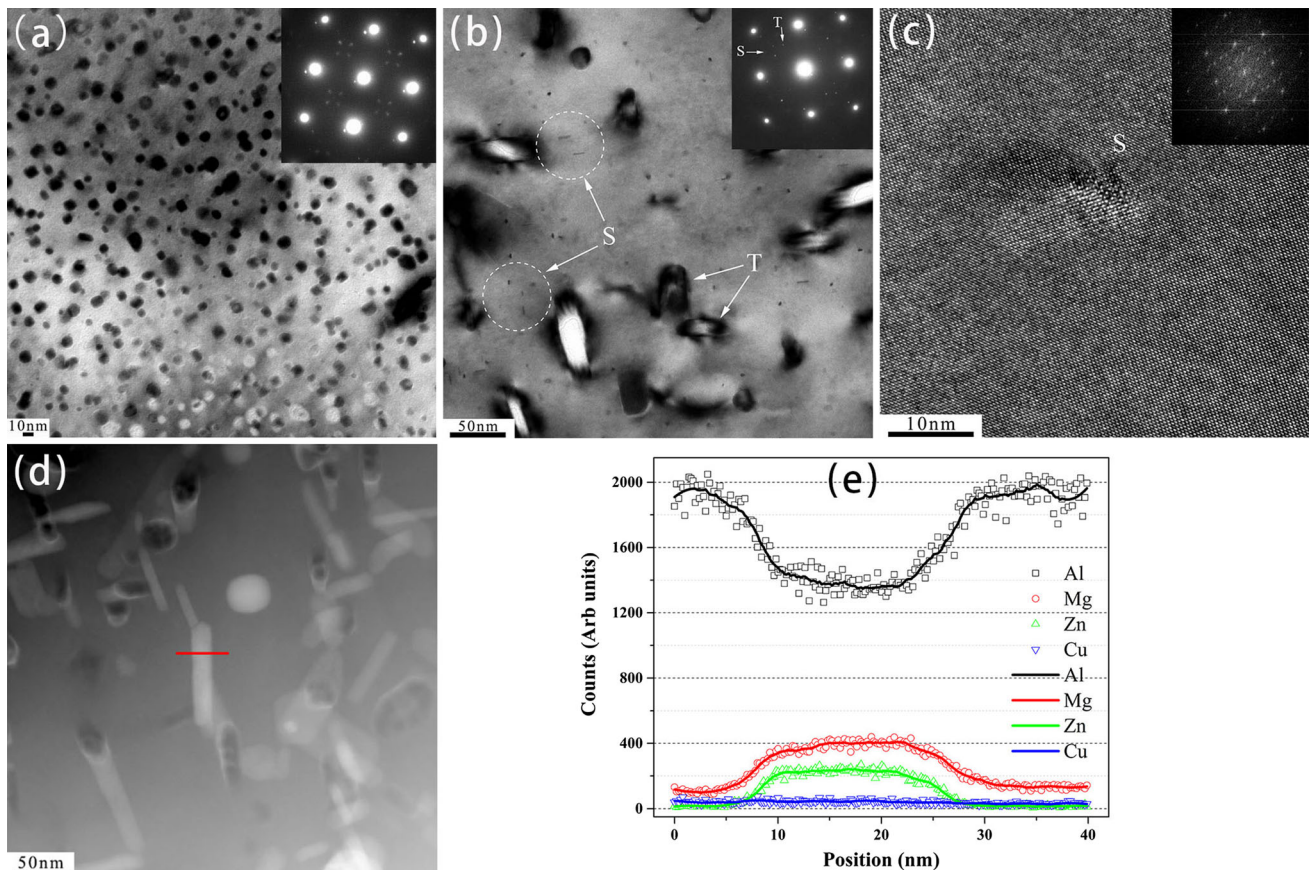


Figure 11 BF TEM (a) for Alloy 2 peak aged at 363 K for 24 h and subsequently aged at 453 K for 2 h. BF TEM (b) and HRTEM image (c), EDS line scan across precipitates (d, e) for Alloy 2 single step aged at 453 K for 10.5 h.

Table 3 Quantitative analysis of the morphology, number density and average diameter of precipitates for Alloy 2 after various aging treatments

Aging treatment	Morphology	Average diameter (nm)	Number density (number/ μm^3)
363 K/24 h	Sphere like	2 ± 0.6	200
363 K/24 h + 413 K/25 h	Sphere like	6 ± 1.8	122
363 K/24 h + 453 K/2 h	Sphere like	10 ± 3.5	33
453 K/10.5 h	T-Mg ₃₂ (AlZn) ₄₉ sphere like S-Al ₂ CuMg fine rod like	T-Mg ₃₂ (AlZn) ₄₉ 27 ± 10.5 S-Al ₂ CuMg 4 ± 1.1	T- Mg ₃₂ (AlZn) ₄₉ 2.1 S-Al ₂ CuMg 7.1
NA/168 h	Sphere like	1.3 ± 0.4	614
NA/720 h	Sphere like	1.5 ± 0.5	633

Discussion

Precipitation behavior of T-Mg₃₂(AlZn)₄₉ phase during artificial aging treatment

The possible precipitation behavior of T phase has been indicated in the Cu-free 7 × × × series Al alloy shown as follows: SSSS → GP zone → intermediate

phase T' → equilibrium phase T-Mg₃₂(AlZn)₄₉ [38], SSSS → solute-vacancy → GP zone → intermediate phase η' or T' → equilibrium phase η or T [39] and SSSS → GP zone → intermediate phase η' → equilibrium phase η → equilibrium phase T [40]. Adding solute atoms with high vacancy binding energy would probably lead to different types of GP zones by increasing the concentration of quenched

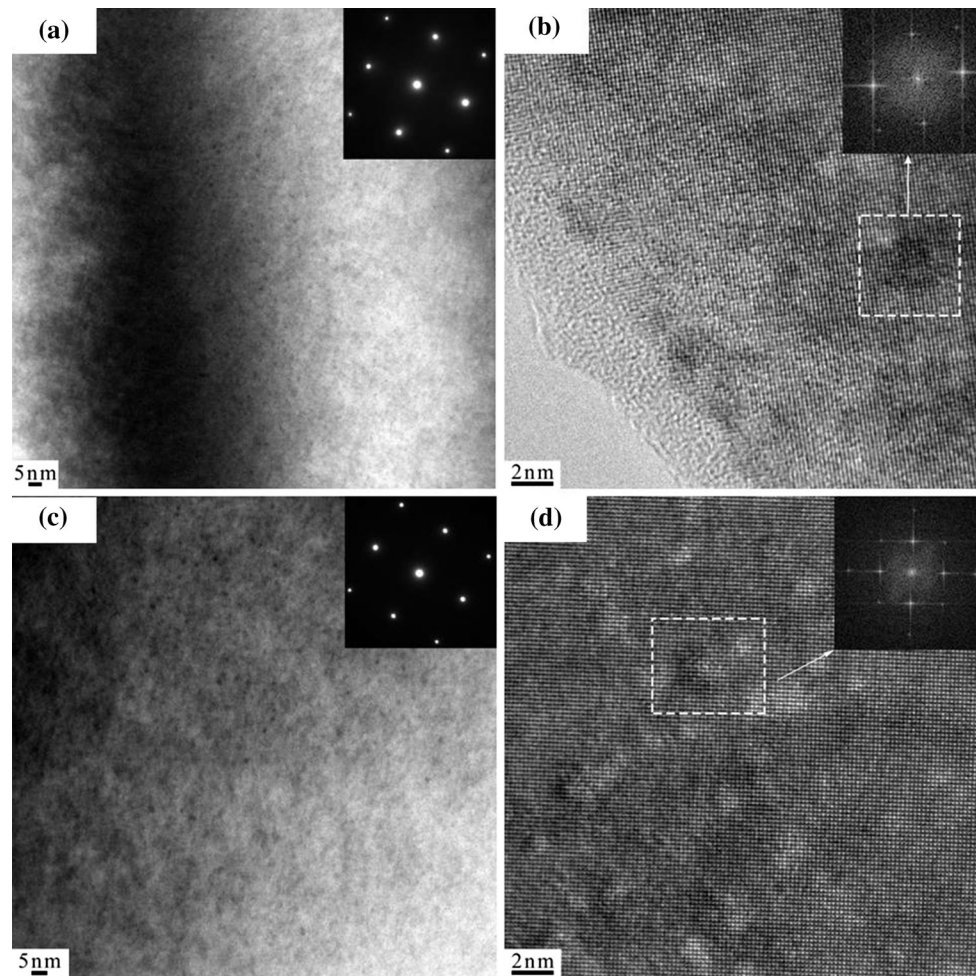


Figure 12 TEM microstructure for Alloy 2 naturally aged for 168 h (a, b) and for 720 h (c, d). a, c BF TEM images; b, d HRTEM images.

vacancies in the Zn-modified Al–Mg alloy. Special precipitation sequences of T phase are also proposed in Al–Mg with Ag addition: SSSS \rightarrow GP zone \rightarrow intermediate phase T' \rightarrow equilibrium phase β -Al₃Mg₂ [21, 41]. The present study provides further evidences to support the precipitation sequence shown in Bigot et al. [34] during artificial aging in an Al–Mg–Zn system: SSSS \rightarrow GP zone \rightarrow intermediate phase T' \rightarrow equilibrium phase T-Mg₃₂(AlZn)₄₉. However, we have got more information about T-Mg₃₂(AlZn)₄₉ and some points are different from previous suggestions.

As shown in Figs. 4, 5, 6 and 7, both GP zones and precipitates with full coherency to the Al matrix are observed in under-aged state. Coherent precipitates with serious lattice distortion are observed in the peak-aged state. Semi-coherent precipitates are observed in over-aged and highly over-aged states.

Incoherent precipitates are expected to be dominated in the highly over-aged alloys. According to the coherent relationship and the results with or without diffraction spots of T phase, the full coherent clusters with no diffraction, full coherent precipitates with diffraction spots, semi-coherent with diffraction spots and incoherent precipitates with diffraction spots are designated as GPI zones, GPII zones (T''), T' and T phases, respectively. In Al alloys with uniformly distributed solute atoms, the precipitation behavior always begins with coherent phase with low interfacial energy and thus low nucleation energy barrier. Based on the current study, the modified precipitation sequence of T phase can be shown as follows: SSSS \rightarrow GPI zone \rightarrow GPII zone (intermediate phase T'') \rightarrow intermediate phase T' \rightarrow equilibrium phase T-Mg₃₂(AlZn)₄₉. This is consistent with the results of DSC curve in as-quenched state after solid solution

treatment as shown in Fig. 9. According to the microstructures in Fig. 7c, d, part of T' precipitates can be transformed into incoherent precipitates even in the highly over-aged state, and we can conclude that semi-coherent T' precipitates are relatively stable during aging treatment. This can also be proved by the fact that dissolution peak D of T' occurs before the peak E. However, previous studies show that fully coherent precipitates are dominant in slightly over-aged state [35], which is different with our results. The Zn–Mg ratio in Yang et al. [35] is much higher than this study. Thus, the reason of the difference may be the composition of T phase. To accelerate the solid phase transformation rate, the precipitation of T phase must depend upon defects such as dislocation loops or voids.

Effects of first-step aging (natural aging or pre-aging) on the subsequently artificial aging treatment

Different effects between natural aging and pre-aging on the subsequently artificial aging treatment

The increased stability of solute-rich GP zones or vacancy-rich GP zones during pre-aging treatment results into the improvement of age-hardening response aged at the second-step treatment for Alloy 2. The stability of GP zones is essentially influenced by both the diameter of particles and the solute supersaturated condition in the matrix. Previous studies showed that in $2 \times \times \times$ or $7 \times \times \times$ series Al alloys, the hardness values can be suddenly increased during second-step artificial aging treatment after natural aging [42, 43]. It means that GP zones of Cu–Mg clusters or Mg–Zn clusters are enough stable during natural aging treatment to prevent dissolution during subsequent artificial aging treatment. On the contrary, Mg–Si clusters in the $6 \times \times \times$ series Al alloy during natural aging are not stable and are easier to dissolve into matrix during subsequent artificial aging treatment [44].

In Fig. 10, our current study demonstrates that the hardness is almost the same during natural aging for 168 h or pre-aging at 363 K for 24 h. After natural aging, the hardness suddenly decreases to a solution-treated value (90 HV) when the alloy is subsequently aged at 453 K within 10 min. However, the hardness increases to a peak value (143 HV) during artificial aging at 453 K for 2 h after first pre-aging at 363 K for

24 h. The most important difference of the microstructure between natural aging and pre-aging at 363 K for 24 h shown in Table 3 lies in the diameter and number density of GP zones or clusters. The average diameter (2 nm) of GP zones during pre-aging at 363 K for 24 h is much larger than those (1.3 nm) naturally aged for 168 h, but the density of the former ($200 \mu\text{m}^{-3}$) is smaller than those (1.3 nm) naturally aged for 168 h ($614 \mu\text{m}^{-3}$). Thus during subsequent artificial aging treatment, the stable GP zones formed during pre-aging are able to grow sufficiently to coherent T'' precipitates. The smaller non-stable clusters formed during natural aging are expected to dissolve into matrix. It is shown that the nucleation of GP zones is stimulated and is easy to grow sufficiently to a size during pre-aging, and they are stable at higher temperature. Previous studies also showed that complete reversion of the hardness did not take place when the first-step aging temperature was higher than 343 K [36]. For these observations, it is probable that critical sizes of precipitates exist at each first-step aging temperature above which the precipitates are stable against dissolution during aging at higher temperature. The critical value for Alloy 2 may be between 1.5 and 2.5 nm. It is also important to know that both the rate and degree of reversion considerably depend upon the first-step aging temperature rather than first-step aging time.

Effects of with or without pre-aging on the subsequently artificial aging treatment

In Fig. 10, pre-aging (363 K for 24 h) can increase peak hardness significantly and improve the age-hardening response greatly during aging at 453 K compared with the single aging at 453 K. The corresponding microstructure results presented in Fig. 11 show that S-Al₂CuMg and T-Mg₃₂(AlZn)₄₉ phases coexist during single-step aging treatment at 453 K, although the content of Cu in the alloy is only 0.15 wt%. However, fine and sphere-like T-Mg₃₂(AlZn)₄₉ precipitates uniformly distribute in the matrix after two-step aging treatment without S-Al₂CuMg phase. Thus we conclude that during single-step artificial aging treatment, the peak hardness is from synergetic effect of coarsening of T phase and hardening of S phase, and during two-step artificial aging treatment, the peak hardness results from a homogeneously distributed T phase in the absence of the S phase.

The diffusion rate of Zn is higher than that of Cu at relatively lower temperature in the matrix [45]. During aging treatment at 363 K for 24 h, Mg–Zn cluster (precursor of T-Mg₃₂(AlZn)₄₉ phase) is much easier to form compared with Mg–Cu cluster (precursor of S-Al₂CuMg phase), and the formation of Mg–Zn cluster consumes a number of Mg atom and inhibits formation of Mg–Cu cluster. As a result, Mg–Zn cluster is the dominant GP zone after pre-aging and T-Mg₃₂(AlZn)₄₉ is the dominant phase when the alloy is subsequently aged at 453 K. This is in accordance with the Cao et al. [46, 47], which showed that the formation of Mg–Zn cluster begins earlier than that of Mg–Cu cluster during aging at 353 K for an Al–5.2Mg alloy containing 0.45 Cu and 2.0 Zn.

Precipitation of S phase appeared only when the aging temperature was over 413 K [42]. In an Al–Zn–Mg–Cu alloy at lower aging temperatures, the content of Cu in precipitates was close to that in the matrix, and it was increasing with an increase of aging temperature and content of Cu in the alloy. This may be caused by the fact that diffusion constants of Mg and Zn in Al is much higher than that of Cu, and the diffusion of Cu in Al depends on aging temperature rather than aging time [48]. In our study, the relatively higher aging temperature (453 K) results in higher diffusion rate of Cu atom, which is favor to the formation of Mg–Cu clusters. In addition, the precipitation of T phase requires long aging time due to the significant high activation energy of T phase formation and the large size of the critical nucleus of T phase [18, 30]. Thus, S-Al₂CuMg and T-Mg₃₂(AlZn)₄₉ precipitates coexist during single-step aging treatment at 453 K, although the content of Cu in Alloy 2 is only 0.15 wt%.

In Figs. 8 (with pre-aging) and 11 (without pre-aging), two kinds of T phase have the same crystal structure, but they contain different elements. The T phase contains Al, Mg, Zn and Cu in Fig. 8 (with pre-aging); however, it contains Al, Mg and Zn without Cu in Fig. 11 (without pre-aging). During pre-aging, the formation of Mg–Zn cluster consumes a number of Mg atoms and inhibits formation of Mg–Cu clusters; however, Cu in matrix can diffuse into T phase during subsequently aging at 453 K. During single-step aging at 453 K, the Mg–Cu clusters form earlier than Mg–Zn clusters and the Alloy 2 only has 0.15Cu (wt%). As a result, most of Cu is in S-Al₂CuMg and there is no obvious Cu in T phase in this state.

Further studies will be carried out to elaborate the synergistic effect of Zn and Cu addition.

Conclusion

This paper systematically investigates the precipitation hardening behavior of Al–5.1Mg–0.15Cu–3.0Zn alloy during different aging treatments. The main points are concluded as follows:

1. The Al–5.1Mg–0.15Cu–3.0Zn alloy possesses higher strength compared with traditional Zn-free alloy (Al–5.1 Mg–0.15Cu alloy), when the alloy is heat-treated at 363 K for 24 h and subsequently aged at 413 K for 25 h. The precipitation sequence of T phase is modified as: SSSS → GPI zone → GPII zone (intermediate phase T'') → intermediate phase T' → equilibrium phase T-Mg₃₂(AlZn)₄₉.
2. First-step aging at 363 K for 24 h produces stable GP zones, which will increase mechanical properties of the alloy during subsequent artificial aging at higher temperatures. On the contrary, the formation of non-stable GP zones or clusters during natural aging results into reversion of mechanical properties during subsequent artificial aging treatment.
3. During single-step artificial aging treatment, the peak hardness is from synergetic effect of coarsening of T phase and hardening of S phase. During two-step artificial aging treatment, the peak hardness results from a homogeneously distributed T phase in the absence of the S phase. Two types of T phase have the same crystal structure and different elements.

Acknowledgements

The authors are grateful to the Major State Research and Development Program of China (No. 2016YFB0300801), the National Natural Science Foundation of China (Nos. 51571013 and 51301017) and projects supported by the Beijing Laboratory of Metallic Materials and Processing for Modern Transportation, China, for the financial support to this study. We would like to appreciate Dr. Zhiwei Du at General Research Institute for Nonferrous

Metals for the help on TEM and HRTEM experiments.

References

- [1] Benedyk JC (2009) International temper designation systems for wrought aluminum alloys: part 1—Strain hardenable (H Temper) aluminum alloys. *Light Metal Age* 26–30
- [2] Showalter DD, Placzankis BE, Burkins MS (2008) Ballistic performance testing of aluminum alloy 5059-H131 and 5059-H136 for armor applications. *Army Res Lab* 1–26
- [3] Komarova MF, Buinov NN, Kaganovich LI (1973) Microstructure and corrosion resistance of an aluminium-magnesium alloy after long-time natural ageing. *Phys Met Metall* 36:358–364
- [4] Boucheur M, Hamana D, Laoui T (1996) GP zones and precipitate morphology in aged Al–Mg alloys. *Philos Mag A* 73:1733–1740
- [5] Yi G, Cullen DA, Littrell KC, Golumbskie W, Sundberg E, Free ML (2017) Characterization of Al–Mg alloy aged at low temperatures. *Metall Mater Trans A* 48:2040–2050
- [6] Yuan Y (2006) Localized corrosion and stress corrosion cracking of Al–Mg alloys. Ph.D. dissertation, University of Birmingham
- [7] Huskins EL, Cao B, Ramesh KT (2010) Strengthening mechanisms in an Al–Mg alloy. *Mater Sci Eng A* 527:1292–1298
- [8] Yin ZM, Jiang F, Pan QL et al (2003) Microstructures and mechanical properties of Al–Mg and Al–Zn–Mg based alloys containing minor scandium and zirconium. *Trans Nonferrous Met Soc China* 13:515–520
- [9] Fu L, Peng Y, Huang J, Deng Y, Yin Z (2015) Microstructures and mechanical properties of gas tungsten arc welded joints of new Al–Mg–Sc and Al–Mg–Er alloy plates. *Mater Sci Eng A* 620:149–154
- [10] Deng Y, Peng B, Xu G et al (2015) Stress corrosion cracking of a high-strength friction-stir-welded joint of an Al–Zn–Mg–Zr alloy containing 0.25 wt% Sc. *Corros Sci* 100:57–72
- [11] Song M, Du K, Huang ZY, Huang H, Nie ZR, Ye HQ (2014) Deformation-induced dissolution and growth of precipitates in an Al–Mg–Er alloy during high-cycle fatigue. *Acta Mater* 81:409–419
- [12] Yang D, Li X, He D, Nie Z, Huang H (2012) Microstructural and mechanical property characterization of Er modified Al–Mg–Mn alloy tungsten inert gas welds. *Mater Des* 34:655–659
- [13] Nie ZR, Li BL, Wang W et al (2007) Study on the Erbium strengthened aluminum alloy. *Mater Sci Forum* 546–549:623–628
- [14] Ratchev P, Verlinden B, de Smet P, Van Houtte P (1998) Precipitation hardening of an Al–4.2 wt%Mg–0.6 wt% Cu alloy. *Acta Mater* 46:3523–3533
- [15] Ratchev P, Verlinden B, De Smet P, Van Houtte P (1998) Effect of cooling rate and predeformation on the precipitation hardening of an Al–4.2 wt%Mg–0.6 wt% Cu alloy. *Scr Mater* 38:1195–1201
- [16] Patchev P, Verlinden B, De Smet P, Van Houtte P (1999) Artificial ageing of Al–Mg–Cu alloys. *Mater Trans JIM* 40:34–41
- [17] Zhu Z, Starink MJ (2008) Solution strengthening and age hardening capability of Al–Mg–Mn alloys with small additions of Cu. *Mater Sci Eng A* 488:125–133
- [18] Li C, Sha G, Gun B et al (2013) Enhanced age-hardening response of Al–4Mg–1Cu (wt%) microalloyed with Ag and Si. *Scr Mater* 68:857–860
- [19] Gupta AK, Chaturvedi MC, Jena AK (1989) Effects of silicon additions on ageing behaviour of Al–1.52Cu–0.75Mg alloy. *Mater Sci Technol* 5:52–55
- [20] Hutchinson CR, Ringer SP (2000) Precipitation processes in Al–Cu–Mg alloys microalloyed with Si. *Metall Mater Trans A* 31:2721–2733
- [21] Kubota M, Muddle BC (2005) Effect of trace additions of Ag on precipitation in Al–Mg alloys. *Mater Trans* 46:2968–2974
- [22] Hirose S, Omura T, Sato T, Suzuki Y (2005) Effects of Ag addition on age-hardening and nano-scale precipitate microstructures of an Al–3%Mg–1%Cu alloy. *J Jpn Inst Light Met* 56:673–679
- [23] Mihara M, Kobayashi E, Sato T (2014) Nanocluster formation and two-step aging behavior of rapid hardening Al–Mg–Cu(–Ag) Alloys. *Mater Sci Forum* 794–796:996–1001
- [24] Mihara M, Marioara CD, Andersen SJ, Holmestad R, Kobayashi E, Sato T (2016) Precipitation in an Al–Mg–Cu alloy and the effect of a low amount of Ag. *Mater Sci Eng A* 658:91–98
- [25] Park M, Terada D, Marya M, Tsuji N (2014) Microstructures and mechanical properties of an artificially-aged Al–Mg–Ga alloy. *Mater Sci Forum* 794–796:1032–1037
- [26] Ding XP, Cui H, Zhang JX et al (2015) The effect of Zn on the age hardening response in an Al–Mg–Si alloy. *Mater Des* 65:1229–1235
- [27] Guo MX, Zhang XK, Zhang JS, Zhuang LZ (2017) Effect of Zn addition on the precipitation behaviors of Al–Mg–Si–Cu alloys for automotive applications. *J Mater Sci* 52:1390–1404. <https://doi.org/10.1080/14786435.2014.913819>
- [28] Carroll MC, Gouma PI, Mills MJ, Daehn GS, Dunbar BR (2000) Effects of Zn additions on the grain boundary precipitation and corrosion of Al–5083. *Scr Mater* 42:335–340

- [29] Carroll MC, Gouma PI, Daehn GS, Mills MJ (2001) Effects of minor Cu additions on a Zn-modified Al-5083 alloy. *Mater Sci Eng A* 319:425–428
- [30] Suzuki Y, Hibino A, Muramatsu T, Hirosawa S, Sato T (2004) Bake-hardenability of Al–Mg–Cu–X (Ag, Zn, Si) alloy sheets. *Mater Sci Forum* 28:258–263
- [31] Matsumoto K, Aruga Y, Tsuneishi H, Iwai H, Mizuno M, Araki H (2014) Effects of Zn addition and aging condition on serrated flow in Al–Mg alloys. *Mater Sci Forum* 794–796:483–488
- [32] Matsumoto K, Aruga Y, Tsuneishi H, Iwai H, Mizuno M, Araki H (2016) Effects of precipitation state on serrated flow in Al–Mg(–Zn) alloys. *Mater Trans* 57:1101–1108
- [33] Sheppard T (1999) *Extrusion of aluminum alloys*, 1st edn. Springer, Berlin
- [34] Bigot A, Auger P, Chambrelan S, Blavette D, Reeves A (1997) Atomic scale imaging and analysis of T' precipitates in Al–Mg–Zn alloys. *Microsc Microanal Microstruct* 8:103–113
- [35] Yang XB, Chen JH, Liu JZ, Qin F, Xie J, Wu CL (2014) A high-strength Al–Zn–Mg alloy hardened by the T-phase precipitates. *J Alloy Compd* 610:69–73
- [36] Löffler H, Kovacs I, Lendvai J (1983) Decomposition processes in Al–Zn–Mg alloys. *J Mater Sci* 18:2215–2240. <https://doi.org/10.1007/BF00541825>
- [37] Meng C, Zhang D, Cui H, Zhuang L, Zhang J (2014) Mechanical properties, intergranular corrosion behavior and microstructure of Zn modified Al–Mg alloys. *J Alloy Compd* 617:925–932
- [38] Polmear LJ (1995) *Light alloys: metallurgy of the light alloys*, 3rd edn. Arnold, London
- [39] Afify N, Gaber A, Abbady G (2011) Fine scale precipitates in Al–Mg–Zn alloys after various aging temperatures. *Mater Sci Appl* 2:427–434
- [40] Inoue H, Sato T, Kojima Y, Takahashi T (1981) The temperature limit for GP zone formation in an Al–Zn–Mg alloy. *Metall Trans A (Phys Metall Mater Sci)* 12A:1429–1434
- [41] Kubota M (2005) Identification of β phase particles in an isothermally aged Al–10 mass%Mg–0.5 mass%Ag alloy. *Mater Trans* 46:2437–2442
- [42] Ringer SP, Caraher SK, Polmear IJ (1998) Response to comments on cluster hardening in an aged Al–Cu–Mg alloy. *Scr Mater* 39:1559–1567
- [43] Huang ZW, Loretto MH, Smallman RE, White J (1994) The mechanism of nucleation and precipitation in 7075–0.7Li alloy. *Acta Metall Mater* 42:549–559
- [44] Zandbergen MW, Xu Q, Cerezo A, Smith GDW (2015) Study of precipitation in Al–Mg–Si alloys by atom probe tomography I. Microstructural changes as a function of ageing temperature. *Acta Mater* 101:136–148
- [45] Bakker H, Bonzel HP, Bruff CM et al (1990) *Diffusion in solid metals and alloys*. Springer, Berlin
- [46] Cao C, Zhang D, He Z, Zhuang L, Zhang J (2016) Enhanced and accelerated age hardening response of Al–5.2Mg–0.45Cu (wt%) alloy with Zn addition. *Mater Sci Eng A* 666:34–42
- [47] Cao C, Zhang D, Zhuang L, Zhang J (2017) Improved age-hardening response and altered precipitation behavior of Al–5.2Mg–0.45Cu–2.0Zn (wt%) alloy with pre-aging treatment. *J Alloy Compd* 691:40–43
- [48] Marlaud T, Deschamps A, Bley F, Lefebvre W, Baroux B (2010) Influence of alloy composition and heat treatment on precipitate composition in Al–Zn–Mg–Cu alloys. *Acta Mater* 58:248–260